Observed Interannual Variability in the Hadley Circulation and Its Connection to ENSO

ABRAHAM H. OORT

Geophysical Fluid Dynamics Laboratory/NOAA, Princeton University, Princeton, New Jersey

JAMES J. YIENGER

Atmospheric and Oceanic Sciences Program, Princeton University, Princeton, New Jersey

(Manuscript received 1 March 1995, in final form 2 April 1996)

ABSTRACT

Based on a 26-yr set of daily global upper-air wind data for the period January 1964–December 1989, the interannual variability in the strength of the tropical Hadley cells is investigated. Although several measures of the intensity of the zonal-mean cells are discussed, the main focus is on the maximum in the streamfunction in the northern and southern Tropics. The streamfunction was computed from observed monthly mean latitude versus pressure cross sections of the zonal-mean meridional wind component. Significant seasonal variations are found in the strength, latitude, and height of the maximum streamfunction for both Hadley cells. Significant correlations are also observed between the Hadley cells and the El Niño–Southern Oscillation phenomenon. During the extreme seasons, only one "winter" Hadley cell dominates the Tropics, with the rising branch in the summer hemisphere and the sinking branch in the winter hemisphere. Superimposed on this "normal" one-cell winter Hadley circulation in the Tropics are two strengthened direct (i.e., energy releasing) Hadley cells found during episodes of warm sea surface temperature anomalies in the eastern equatorial Pacific (El Niño) and weakened Hadley cells during episodes of cold anomalies. The anomalies in the strength of the Hadley cells are strongly and inversely correlated with the anomalies in the strength of the Walker oscillation.

1. Introduction

There are many well-established links between oceanic and atmospheric phenomena. Probably the most notable link is the El Niño/Southern Oscillation, in which there is a close correlation between temperature anomalies in the eastern equatorial Pacific and anomalies in the Walker oscillation (WO) (Bjerknes 1969). Researchers have shown that sea surface temperature anomalies in the eastern equatorial Pacific are also correlated with other, more remote, atmospheric features such as the subtropical jets, the subtropical high over the western and central Pacific, and the Aleutian low (e.g., Arkin 1982; Rasmusson and Carpenter 1982; Pan and Oort 1983). In this paper, we illustrate a connection between ENSO and the tropical zonal-mean Hadley circulation using a 26-year set of global upper-air wind data for the period January 1964–December 1989.

2. Data and method of analysis

The time series of 26 years of monthly data for three parameters were analyzed and cross correlated: the maximum value of the streamfunction in the Northern and Southern Hemispheric Tropics (a Hadley circulation index), the difference between the eastern equatorial Pacific (EEP) and the western equatorial Pacific (WEP) vertical velocities at 500 mb (a Walker oscillation index), and the sea surface temperature anomalies of the EEP (an ENSO index). Each index is discussed briefly below. The atmospheric wind data used here are part of the Geophysical Fluid Dynamics Laboratory Atmospheric Circulation Tape Library [Oort 1983 (updated)]. The objective analysis scheme used to interpolate between the basic monthly mean rawinsonde station data is described in Oort (1983), Rosen et al. (1979), and Raval et al. (1996). A zonal average of the station data in latitudinal belts was used as the first-guess field, leading to some difficulties in data-sparse regions (see Fig. 1) such as the eastern equatorial Pacific Ocean (Raval et al. 1994; Raval et al. 1996). The sea surface temperature and the surface wind data over the oceans were taken from the Comprehensive Ocean–Atmosphere Data Set (COADS; Woodruff et al. 1987) and were interpolated to gridpoint values using the same analysis scheme as was used in the atmosphere.

a. Hadley circulation index

As a simple parameter to gauge the monthly variations in the intensity of the Hadley circulation,

Corresponding author address: Dr. Abraham H. Oort, GFDL/NOAA, Princeton University, Forrestal Campus, U.S. Route 1, Post Office Box 308, Princeton, NJ 08542.

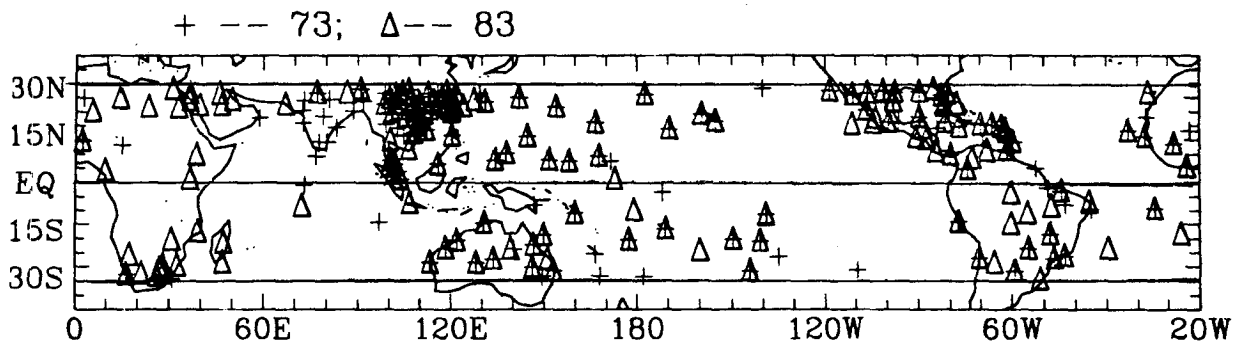

FIG. 1. Horizontal distribution of reliable rawinsonde stations in the 30°S–30°N belt used in the present analyses. The stations are shown both for January 1973 (indicated by plus signs) and January 1983 (indicated by triangles).

we use the strength of the mean meridional overturning of mass in the 0°–30°N zone for the Northern Hemispheric (NH) Hadley cell and in the 0°–30°S zone for the Southern Hemispheric (SH) Hadley cell. The mass transport is computed using observed zonal-mean meridional winds and the zonally averaged mass continuity equation in the form

$$\frac{\partial[\bar{v}]\cos\phi}{R\cos\phi\partial\phi} + \frac{\partial[\bar{\omega}]}{\partial p} = 0, \qquad (1)$$

where v is the meridional velocity, ω is the vertical velocity in pressure coordinates, R is the mean radius of the earth, and p is the pressure. The operators $\bar{\ }$ and $[\ ]$ stand for temporal and zonal averaging, respectively. Introducing a Stokes streamfunction ψ given by the equations

$$[\bar{v}] = g\frac{\partial\psi}{2\pi R\cos\phi\partial p} \qquad (2)$$

$$[\bar{\omega}] = -g\frac{\partial\psi}{2\pi R^2\cos\phi\partial\phi}, \qquad (3)$$

we can compute the ψ field, assuming $\psi = 0$ at the top of the atmosphere and integrating (2) downward to the surface. We will discuss the sign convention used for ψ later in connection with the actual cross sections of ψ.

To ensure vertical-mean mass balance, the $[\bar{v}]$ fields were corrected by removing their mass-weighted vertical mean value $[\hat{\bar{v}}] \equiv \int_0^{p_0}[\bar{v}]dp/p_0$. The 26-yr mean values of $[\hat{\bar{v}}]$ and their standard deviations are presented in Table 1 as a function of latitude. In the Tropics, both the means and standard deviations are on the order of 0.2 to 0.3 m s^{-1} or less. In comparison, the maximum velocities in the Hadley cells are 2 to 3 m s^{-1} (see appendix A, Table A2, lines 8 and 9)—that is, an order of magnitude larger than the residual values. Our residual values are comparable to those presented in Rosen (1976) based on a 10-yr sample. In the same paper, Rosen (1976) also presented an extensive analysis of possible reasons for the nonzero residual values.

The $[\bar{v}]$ data were computed from our $\bar{v}$ analyses and were based on more than 700 reliable rawinsonde stations distributed around the globe. The geographical distributions of the tropical rawinsonde stations used in our analyses are presented for two representative January months in Fig. 1. From this figure one can infer that the rawinsonde network has been relatively stable throughout the 26-yr period of record [see also Oort (1983) for the early years], with the exception of Africa and South America where the network has improved with time. One possible influence on the Hadley circulation may be the better definition of the north-

TABLE 1. The 26-yr mean (1964–89) values of $[\hat{\bar{v}}]$ at various latitudes, used as a measure of the computed net poleward flow of mass, and their standard deviations (based on 312 monthly estimates) in units of m s^{-1}. Since in the case of perfect data $[\hat{\bar{v}}]$ should be close to zero (Rosen 1976), these (spurious) nonzero values are a measure of the uncertainty in the computed $[\hat{\bar{v}}]$.

	Latitude											
	−30°	−20°	−10°	0°	10°	20°	30°	40°	50°	60°	70°	80°
$[\bar{v}]$	0.13	0.04	0.10	0.19	0.02	0.08	0.05	−0.17	−0.17	−0.10	0.02	−0.05
σ	0.34	0.28	0.15	0.12	0.13	0.22	0.24	0.39	0.20	0.12	0.16	0.53

ward Somali jet across the equator during summer in the later years. To remedy this particular situation and to correct, in general, for the sparse distribution of the rawinsonde stations over the oceans, we substituted our analyses of the COADS surface $\bar{v}$ field (Woodruff et al. 1987) for the rawinsonde-based analyses at 1000 mb. This procedure greatly improved the low-level wind analyses over the oceans. The resulting dataset provides reasonable global coverage at 2.5° latitude and 50 mb (50–1000 mb) vertical pressure resolution, except south of 40°S where the data are extremely sparse.

To calculate the mean meridional streamfunction ψ using (2), we zonally averaged the analyzed fields of $\bar{v}$. One should realize, however, that the reliability of the results for the streamfunction must be strongly latitude dependent. Poleward of 30° latitude, the mean meridional velocity $[\bar{v}]$ is a small statistical residue of large, almost compensating, northward and southward flows in the midlatitude quasistationary waves (i.e., in the jet streams we find local $\bar{v}$ velocities ~10–20 m s^{-1}, whereas typical zonal-mean $[\bar{v}]$ velocities in the midlatitudes are ≤0.5 m s^{-1}). Trying to isolate such minuscule velocities is somewhat problematic. Nevertheless, even in midlatitudes, the $[\bar{v}]$ values are larger than the vertical-mean residuals shown in Table 1 (≤0.2 m s^{-1}) and are, therefore, probably of the right sign and magnitude. In the Tropics (30°N–30°S) the $[\bar{v}]$ values are, at least in winter, the direct result of averaging a fairly uniform equatorial Hadley circulation, so that we expect to find more reliable values for the mean meridional streamfunction in the tropical regions. In summer, the zonal symmetry is much disturbed over Southeast Asia, but still the rawinsonde network supplemented by the surface COADS wind data over the oceans seems to be adequate to properly take this factor into account (see Fig. 1). While there is some uncertainty near the latitude of the subtropical jets, integration through the total vertical column to calculate the mass streamfunction should also smooth out some of the possible noise in $[\bar{v}]$, leading perhaps to a more stable measure in the ψ parameter.

b. *Walker oscillation index*

The Walker oscillation is one of the primary atmospheric components of ENSO (see, e.g., Julian and Chervin 1978; Rasmusson and Carpenter 1982). It is responsible for large east–west shifts of atmospheric mass between the Indian and west Pacific Oceans on the one side and the east Pacific Ocean on the other side. The Walker oscillation is a circulation in the east–west vertical plane characterized during "average" conditions by rising motions over the western equatorial Pacific (WEP) and Indian Oceans and sinking motions over the eastern equatorial Pacific Ocean (see Table A3, quantities 11–13). However, during El Niño conditions, anomalous warming of the EEP and anomalous cooling of the WEP weakens and sometimes even reverses the Walker oscillation, leading to anomalous dry conditions in the west and wet conditions in the east. Because the well-organized vertical motions in the east and west branches are a key aspect of the Walker oscillation, we defined the Walker oscillation index as the difference in vertical velocity at 500 mb between the EEP (averaged over the area 10°N–10°S, 180°–100°W) and the WEP (averaged over the area 10°N–10°S, 100°–150°E). The Walker oscillation index is not sensitive to the details of the choice of area. To compute the vertical pressure velocity ω ($\equiv dp/dt$), we used the continuity equation for mass together with our global field of rawinsonde horizontal velocities:

$$\omega(p) = -\int_0^p \mathrm{div} V dp, \tag{4}$$

where $V(u, v)$ is the horizontal velocity vector, while making sure that

$$\omega(p_0) = -\int_0^{p_0} \mathrm{div} V dp = 0 \tag{5}$$

for vertical mass flux balance. In requiring $\omega = 0$ at both the top surface ($p = 0$) and at the earth's surface ($p = p_0$), possible (usually small) nonzero values of $\omega(p_0)$ in the vicinity of mountains are neglected. Considering the station distribution shown in Fig. 1, we note that there are only a few rawinsonde stations located inside the EEP region as defined here. However, the influence of the more plentiful stations between 10° and 20° latitude, both north and south, helps to alleviate much of the problem of computing the mean divergence and ω averaged over the area.

c. *El Niño index*

We used the monthly mean analyses of the COADS sea surface temperatures by Pan and Oort (1983) for the same 26-year period to compute monthly anomalies in the EEP (averaged over the area 20°N–20°S, 180°–80°W) as an index of El Niño (warm) conditions and La Niña (cold) conditions in the eastern equatorial Pacific. A similar index was used extensively in some of our previous work (e.g., Pan and Oort 1983). The EEP averages represent approximately the mean conditions over regions Niño 3 and Niño 4 [see Rasmusson and Carpenter (1982) and recent issues of the *Climate Diagnostics Bulletin*], generally accepted as a representative measure of El Niño.

3. Long-term mean climatology

a. *Annual cycle*

In Figs. 2 and 3 we present the 26-yr mean annual and monthly cross sections of the zonal-mean mass streamfunctions for the 30°S–80°N area. We use here a positive sign for the streamfunction ψ in the case of a clockwise rotation and a negative sign for an anti-

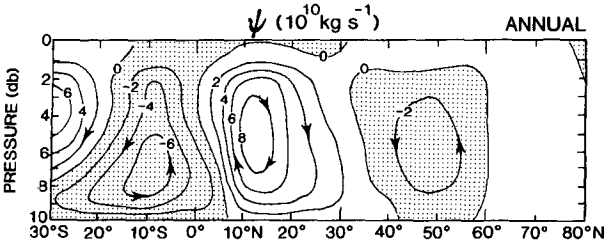

FIG. 2. Cross section of the zonal-mean mass streamfunction ψ for annual-mean conditions in units of 10^{10} kg s^{-1} based on 1964–89 data. Over the entire domain of 30°S–80°N, the streamfunction was computed *directly* from the observed mean meridional component of the wind $[\bar{v}]$, with the only imposed constraint being that $\int_0^{p_0} [\bar{v}]dp = 0$ to ensure conservation of mass.

clockwise rotation, as seen in the (p, ϕ) cross sections in Figs. 2 and 3. The difference $\psi_1 - \psi_2$ between two points on a cross section is equal to the amount of mass flowing across a line joining the two points. Thus, the annual maximum ψ value of 9.2 for the NH Hadley cell in Fig. 2 indicates that an amount of mass of 9.2×10^{10} kg s^{-1} is transported northward above the level of maximum ψ and an equal amount southward below it. Analogously, for the SH Hadley cell we find a minimum value of -7.4×10^{10} kg s^{-1}, indicating that this amount of mass is flowing southward above the level of minimum ψ and an equal amount northward below it. According to this sign convention, strengthening of the two tropical Hadley cells would mean larger positive values of ψ in the NH Tropics and more negative values of ψ in the SH Tropics.

Although the tropical annual-mean values represent small residuals of two opposing Northern and Southern Hemispheric winter Hadley circulations, Fig. 2 shows in a clear way the "idealized" long-term mean meridional overturnings in the atmosphere. We note the existence of two almost symmetrical tropical Hadley cells, a weak Ferrel cell in the midlatitudes, and a still weaker polar cell.

Figure 3 shows that maximum mass overturning occurs at the center of the wintertime NH and SH Hadley cells. Both ψ^N and ψ^S (see definitions in appendix A, Table A1) reach a sharp peak during the corresponding winter months and decline to near-zero values during the summer months. As has been shown before (see, e.g., Oort and Rasmusson 1970; Newell et al. 1972), the typical, idealized representation of the tropical-mean meridional circulations as two equal-strength Hadley cells is in reality a rarity. One hemisphere tends to dominate during most of the year, with the transition period (the time when ψ^N and ψ^S are about equal) being at most 2 months between winter and summer. The absolute values of the 3-month averages of the extremes in the streamfunction in both hemispheres are on the order of 20×10^{10} kg s^{-1} in winter and 2 to 3 $\times 10^{10}$ kg s^{-1} in summer, while the annual average is only $\sim 11 \times 10^{10}$ kg s^{-1} (see Table A2, lines 2 and 3). (Please note that the extreme values shown in Fig. 2 are smaller than 11×10^{10} kg s^{-1} because of the difference in defining the mean of the seasonal values and the annual mean; see appendix A.) The midlatitude Ferrel cell also exhibits a pronounced annual variation, being strongest in winter, as expected from the increase in baroclinic disturbances during that season.

For further, more quantitative information on the long-term (26 yr) mean and interannual standard deviation values of the maximum streamfunction, as well as on a variety of other parameters characterizing the Hadley cells and the Walker oscillation, the reader is referred to the extensive tabulations in appendix A.

b. *Stability of the results*

Similar results as shown in Figs. 2 and 3 for the annual and monthly mean conditions were obtained by Oort and Rasmusson (1970) and Newell et al. (1972), among others. However, these studies were based on shorter data samples. It is interesting to note that Newell et al. (1972) find a slightly stronger Hadley cell in northern summer than in northern winter, contrary to our findings in Fig. 3. This difference may be considered to be a measure of the uncertainty in estimating the mean cell intensities. On the other hand, more important for the fluxes of water vapor and energy is the fact that in *both* datasets the June–August (JJA) cell extreme is located at much lower elevation than in the December–February (DJF) case, leading to stronger fluxes during JJA. We will come back to this issue later. At the left-hand side of the diagrams in Figs. 2 and 3, south of about 20°S, we find evidence of an intrusion by a much-too-strong SH Ferrel cell. Apparently, the station distribution is not adequate at these latitudes to get reliable estimates of the mean meridional circulation.

To further study the stability of the zonal-mean streamfunction fields presented in Figs. 2 and 3, we have computed the standard deviation $\sigma(\psi)$ based on the 26 years of data. The results for January and July are shown in Fig. 4. We find that in the Tropics at the location of the maximum streamfunction $\sigma(\psi) \approx 3 \times 10^{10}$ kg s^{-1}. Assuming a Gaussian distribution, this would correspond to a standard error of the mean $\sigma/(N)^{1/2} = 3/(26)^{1/2} \approx 0.6 \times 10^{10}$ kg s^{-1} and would lead to the conclusion that our estimates of the mean streamfunction are known with an uncertainty of $\pm 1 \times 10^{10}$ kg s^{-1}. However, this is probably an underestimate because of other uncertainties related to the nonuniform station distribution and the analysis techniques used. For example, Starr et al. (1970) have shown that the values of the streamfunction can be very sensitive to the analysis technique used, especially to the choice of initial-guess field. Of course the spread in individual monthly estimates of ψ^N and ψ^S is much greater (see, e.g., Fig. 5), since it is given by $\pm 2\sigma$ rather than by $\pm 2\sigma/(N)^{1/2}$.

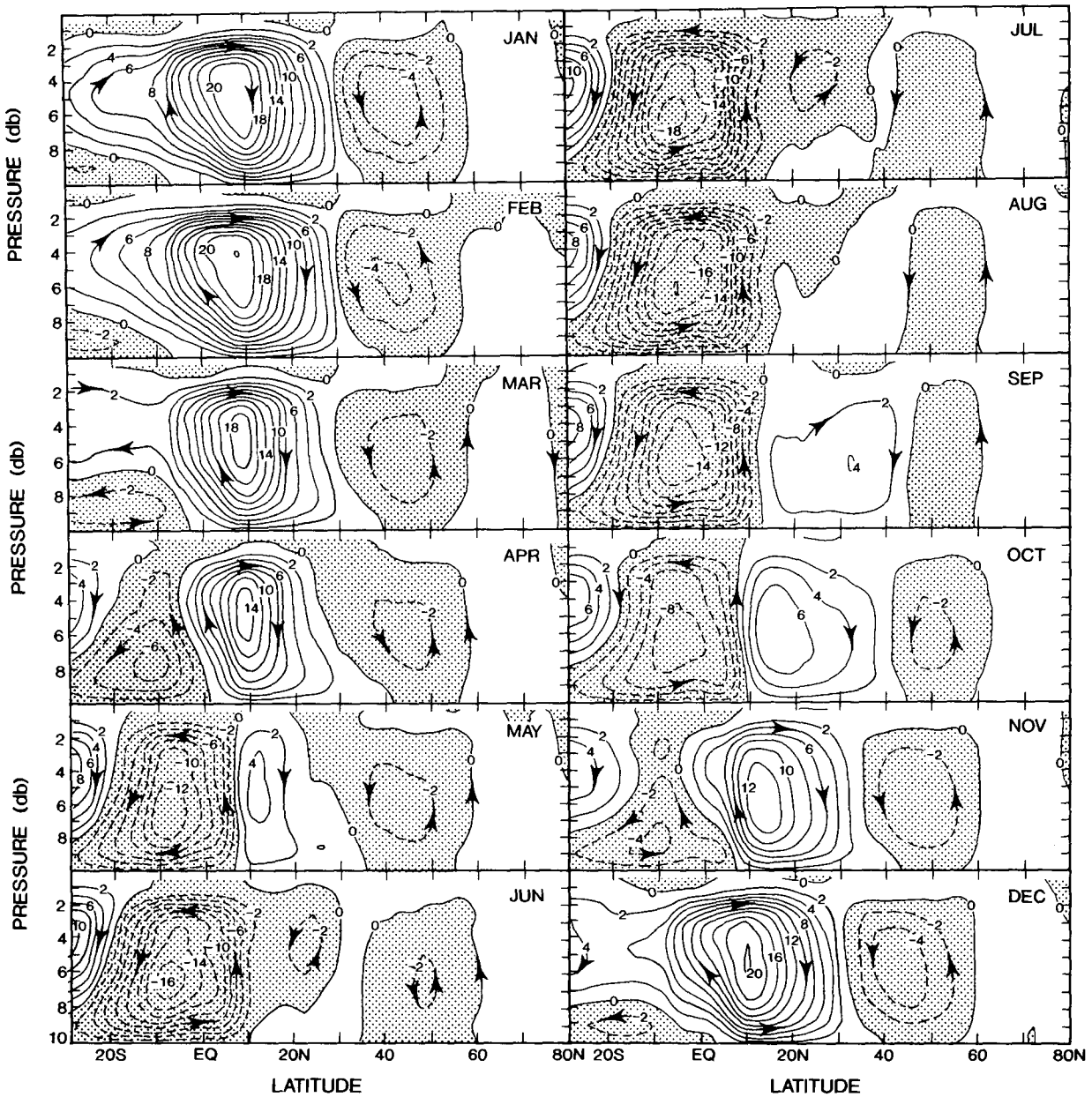

FIG. 3. Annual cycle of the zonal-mean mass streamfunction ψ in units of 10^{10} kg s^{-1} for the 1964–89 mean conditions (see also Fig. 1 caption).

c. Implied transports of water vapor

Going back to Fig. 2, the maximum mass overturning in the Northern Hemisphere ($\sim 9 \times 10^{10}$ kg s^{-1}) was found to be about 20% stronger, on average, than in the Southern Hemisphere ($\sim -7 \times 10^{10}$ kg s^{-1}). This difference in maximum mass overturning of the two cells is interesting considering that more precipitation is observed annually in the NH Tropics (associated with the deep penetration of the SH Hadley cell into the NH during JJA) than in the SH Tropics (Peixoto and Oort 1992). Although the annual-mean SH Hadley cell is found to be weaker than its NH counterpart, it penetrates across the equator to ~7°N at the surface and its center is located closer to the ground (averaging about 750 mb in the SH and 550 mb in the NH). Since atmospheric moisture is much more abundant near the surface, the weaker SH Hadley circulation is therefore found to transport more water vapor across the equator into the NH. To show this more quantita-

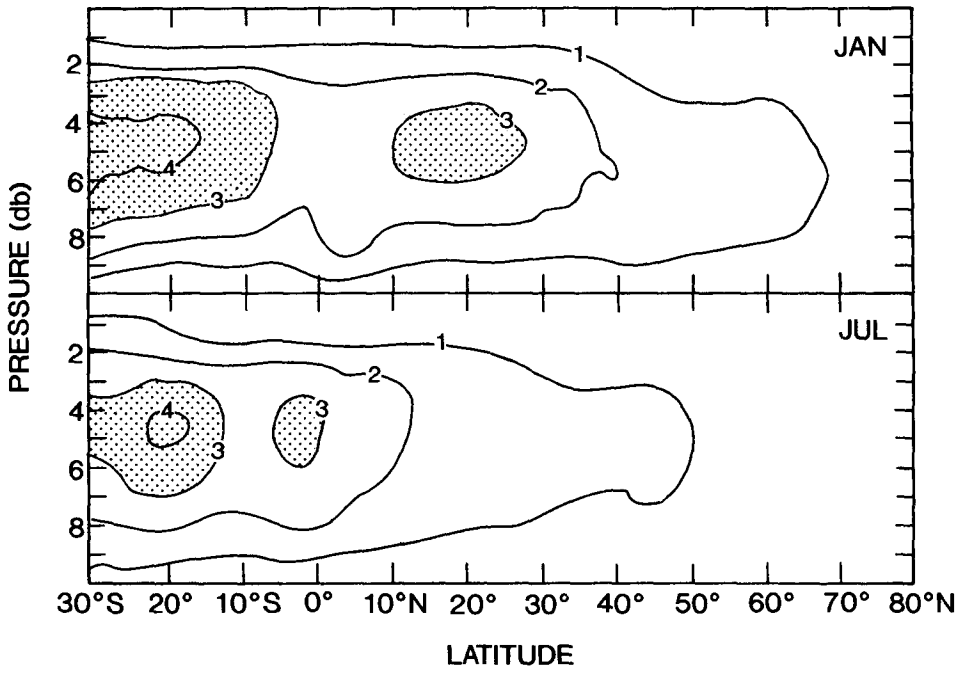

FIG. 4. Interannual standard deviation of the zonal-mean mass streamfunction $\sigma(\psi)$ for January and July in units of 10^{10} kg s^{-1}.

tively, we have computed the water vapor transport F_q across various latitudinal "walls" associated with the mean meridional circulation, using the expression

$$F_q = 2\pi R \cos\phi \int_0^{p_0} [\bar{v}][\bar{q}] \frac{dp}{g}, \qquad (6)$$

where q is the specific humidity. Some of the results are tabulated in appendix A, Table A3 (quantities 3–6). In agreement with our earlier discussion, the average cross-equatorial northward flux of water vapor during JJA (associated with the SH winter Hadley cell) is northward and equals $\sim 21 \times 10^8$ kg s^{-1}, whereas the corresponding southward flux of water vapor during DJF is only -10×10^8 kg s^{-1} (associated with the NH winter Hadley cell). The annual flux is northward and has a value of 6.5×10^8 kg s^{-1} (see also Peixoto and Oort 1992).

The corresponding estimates for the fluxes of energy by the Hadley cells are also of considerable interest. However, to keep the present discussion focussed on the mass streamfunction, the discussion of the implied energy transports is postponed to the appendix.

4. Interannual variations

a. *Hadley–ENSO time series*

An early attempt to document the interannual variability in the mean meridional circulations was made by Rosen et al. (1976) for the period 1958–68. However, these authors limited their study to annual-mean values, which are less reliable than the seasonal values to be shown here.

In Fig. 5 we present monthly time series of the maximum positive ψ in the northern Tropics (0°–30°N) and the minimum negative ψ in the southern Tropics (0°–30°S), irrespective of the latitude of the extreme values (denoted by ψ^N and ψ^S, respectively). Inspection of the curves in Fig. 5 indicates that the wintertime maxima tend to be more peaked and that the summer minima tend to be broader. This suggests that both annual and semiannual harmonics are important in the seasonal cycle.

Using the maximum streamfunction as a representative measure of the strength of the tropical Hadley circulation, we have investigated how the ψ^N and ψ^S time series are correlated with the SST record in the eastern equatorial Pacific. To show these correlations qualitatively, we have removed the 26-year monthly means from the ψ^N and ψ^S time series and plotted them along with the time series of the SST anomalies in Fig. 6 (top and middle diagrams). We note that warm SST anomalies (El Niño events) correspond to a strengthening of ψ^N and ψ^S, and that a weakening of ψ^N and ψ^S occurs during cold SST anomalies (i.e., anti-El Niño, or La Niña events). There is one clear exception to this relationship in the Northern Hemisphere, namely during the strong 1982–83 El Niño event, when ψ^N appears to have weakened. It is peculiar that this anomalous weakening

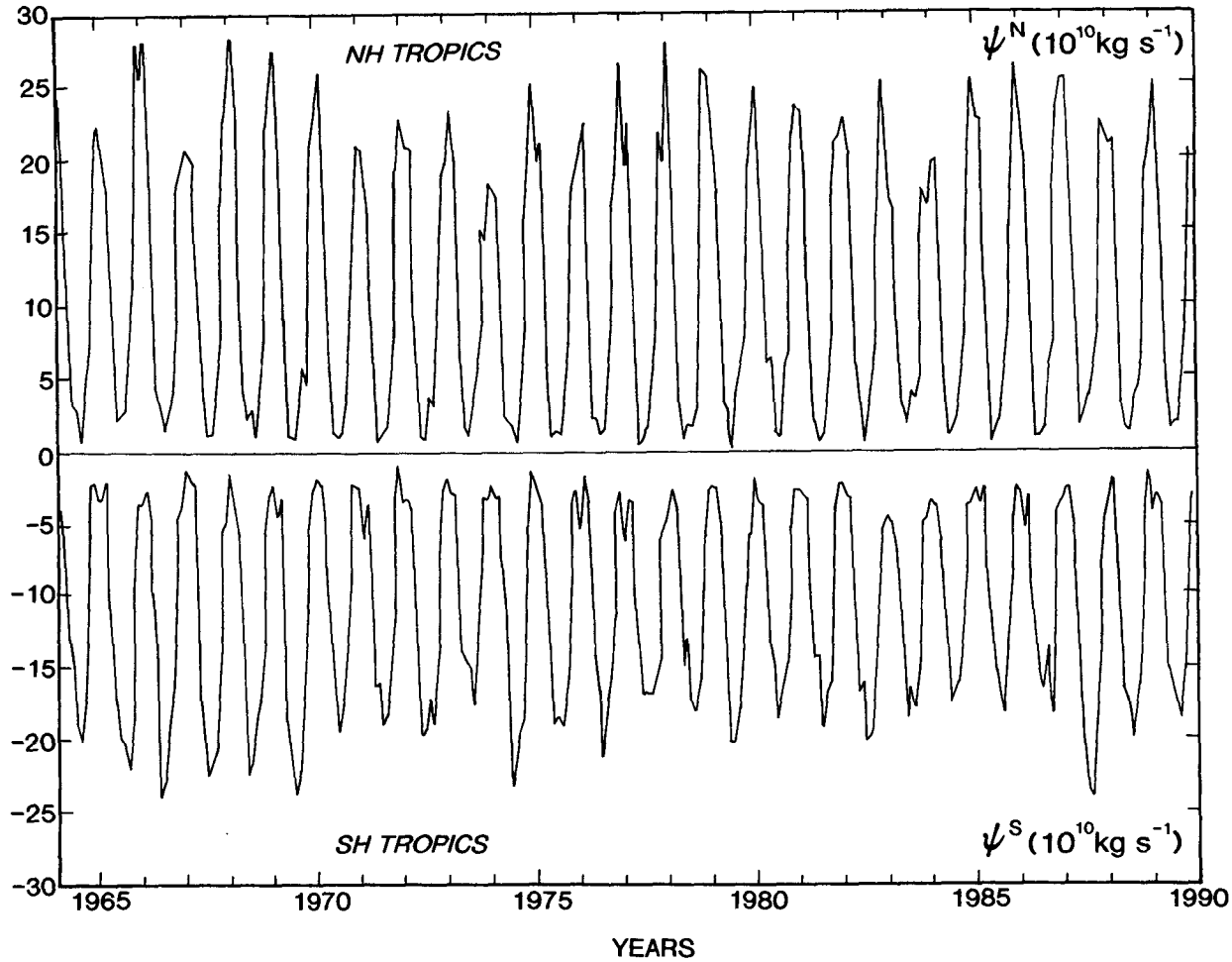

FIG. 5. Time series (unsmoothed) of the maximum values of the mass streamfunction in the northern (top) and southern (bottom) Tropics in units of 10^{10} kg s^{-1}. The tick marks at the bottom and top of the figure indicate the January month for a particular year.

is not observed in the Southern Hemisphere. In fact, at present there is no obvious explanation for these differences, although one possibility is that the northward flow in the 10°–20°N latitude belt moved to the east into the data-sparse region of the eastern equatorial Pacific. The simultaneous correlation between SST anomalies and the smoothed ψ^N anomalies is 0.35, while the correlation with the ψ^S is even more significant at −0.48 (see Table 2). A time-lag analysis to investigate lag relationships was inconclusive.

An extensive tabulation of the correlation coefficients at zero lag between various quantities characterizing the ENSO and WO signals is presented in Table 2 both for smoothed and unsmoothed (between parentheses) conditions. The correlation coefficients that are statistically significant at the 95% confidence level are underlined (see discussion below). The sea surface temperature anomalies in the eastern equatorial Pacific Ocean are used as the basic quantity describing the El Niño/La Niña conditions. The quantities ψ^N, ψ^S, and Δv^N and Δv^S are then used as a measure of the intensity of the tropical Hadley cells, whereas u^N_{200} and u^S_{200} measure the changes in intensity of the subtropical jet as a consequence of changes in the Hadley cells. Variations in the fluxes of water vapor F^N_q and F^S_q, and the resulting precipitation minus evaporation ($P-E$) in the equatorial zone again result from changes in the Hadley cells. The same is true for the energy fluxes F^N_E and F^S_E. Finally, the area-averaged 500-mb vertical velocities in the eastern and western Pacific Ocean measure the intensity of the Walker oscillation.

1) STATISTICAL SIGNIFICANCE OF CORRELATION COEFFICIENTS

To test the statistical significance of the computed correlation coefficients $r(x, y)$ in Table 2, we have used the null hypothesis that the population value

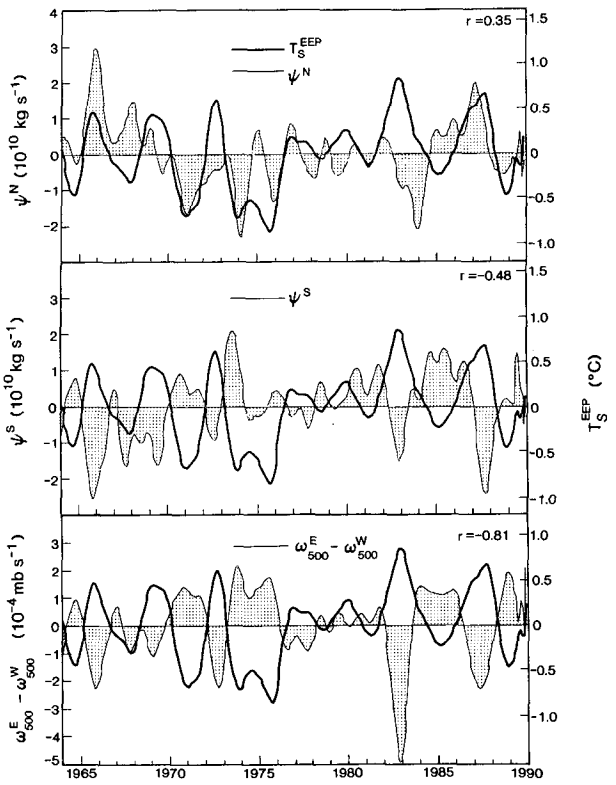

FIG. 6. Time series of the anomalies of the sea surface temperature (thick solid line) in the eastern equatorial Pacific (20°S–20°N, 180°–80°W) as an ENSO index, and of the anomalies of the maximum streamfunction (thin solid line) in the 0°–30°N belt (top figure) and in the 0°–30°S belt (middle figure), used as an index of the strength of the tropical Hadley circulation. The bottom figure shows the time series of the difference in the mean 500-mb vertical (pressure) velocity (thin solid line) in the eastern equatorial Pacific (10°S–10°N, 180°–100°W average) and in the western equatorial Pacific (10°S–10°N, 100°–150°E). A positive value of $\omega^E_{500} - \omega^W_{500}$ indicates a more intense east–west Walker circulation—that is, stronger rising motion over the western portion and stronger sinking over the eastern portion of the equatorial Pacific. All curves are based on the monthly values after smoothing with a 15-month Gaussian filter with weights 0.012, 0.025, 0.040, 0.061, 0.083, 0.101, 0.117, and 0.122 at the central point.

$\rho(x, y) = 0$. Because the sampling distribution of $r(x, y)$ around its population value $\rho(x, y)$ is not normal, we computed confidence limits using the so-called Fisher's Z transformation (Spiegel 1961):

$$Z = \frac{1}{2}\ln\left(\frac{1+r}{1-r}\right). \tag{7}$$

The Z statistic is approximately normally distributed, with a mean value

$$\mu_Z = \frac{1}{2}\ln\left(\frac{1+\rho}{1-\rho}\right) \tag{8a}$$

and a standard deviation

$$\sigma_Z = (N_{df} - 3)^{-1/2}, \tag{8b}$$

where N_{df} is the number of degrees of freedom (Spiegel 1961, pp. 247 and 264). The 95% confidence limits for μ_Z are then given by

$$Z + 1.96\sigma_Z = 0.5\ln\left(\frac{1+r}{1-r}\right) + 1.96(N_{df} - 3)^{-1/2} \tag{9a}$$

and

$$Z - 1.96\sigma_Z = 0.5\ln\left(\frac{1+r}{1-r}\right) - 1.96(N_{df} - 3)^{-1/2}. \tag{9b}$$

To test the null hypothesis we have used (9b) with various values of r and N_{df} to construct Fig. 7. The figure shows a curve ρ_0 separating the areas of significant correlation estimates from those that are insignificant, given by

$$0.5\ln\left(\frac{1+\rho_0}{1-\rho_0}\right) = 0.5\ln\left(\frac{1+r}{1-r}\right) - 1.96(N_{df} - 3)^{-1/2}. \tag{10}$$

The next important issue concerns the choice of the number of degrees of freedom N_{df} appropriate for the various cross-correlation coefficients given in Table 2. In 1963 the late J. Murray Mitchell Jr. [see appendix B, (B12)] showed that when both time series are autocorrelated (as is the case here) the number of degrees of freedom is given by

$$N_{df} = N\left[1 + \frac{2}{N}\sum_{\tau=1}^{N-1}(N - \tau)r_\tau(x)r_\tau(y)\right], \tag{11}$$

where N is the sample size, and $r_\tau(x)$ and $r_\tau(y)$ are the autocorrelation coefficients at lag τ. The corresponding expression in case of the variance of a time series rather than the covariance of two time series has been used frequently. The expression is the same as (11) except for the replacement of $r_\tau(x)r_\tau(y)$ by $r_\tau(x)$ (see, e.g., Jones 1975). We have used (11), including terms of up to 8-months lag, to arrive at stable estimates of N_{df}. The results for N_{df} ranged between 31 and 42 for the smoothed time series and between 61 and 250 for the unsmoothed time series used in computing the correlation coefficients in Table 2. Most of the correlation values presented in the table proved to be significant at the 95% confidence level (see underlined values) based on the method described above.

2) "WARM"–"COLD" CONDITIONS

A measure of the net ENSO influence on the Hadley circulation can also be obtained from Fig. 8 where the differences in ψ between the five warmest El Niño and the five coldest La Niña events are shown both for DJF

TABLE 2. Correlation coefficients at zero lag between different quantities characterizing the ENSO and WO signals. [See Table A1 for the definition of the symbols used. Please note that for most variables, the correlations with ψ^N and ψ^S have the opposite sign; this is, of course, due to the sign convention used for the streamfunction in the two hemispheres (see section 3.1)]. Both smoothed [a 15-point Gaussian-type filter (with weights 0.012, 0.025, 0.040, 0.061, 0.083, 0.101, 0.117, and 0.122 at the central point) was used to filter out high-frequency variations from the monthly data] and unsmoothed (in parentheses) values of the correlation coefficients are presented. Anomalies from the climatological mean are used in all calculations, except in the case of the quantities ω^E_{500}, ω^W_{500}, and $\omega^E_{500} - \omega^W_{500}$ where total values were used, since they show a negligible mean annual variation. Values that were computed to be statistically significant at the 95% confidence level are underlined (see text).

	ψ^N	ψ^S	Δv^N	Δv^S	Δv^N_{PAC}	Δv^S_{PAC}	u^N_{200}	u^S_{200}	F^N_q	F^{eq}_q	F^S_q	$P - E$	F^N_E	F^{eq}_E	F^S_E	div F_E	ω^E_{500}	ω^W_{500}	$\omega^E_{500} - \omega^W_{500}$
T_S	0.35	−0.48	0.49	−0.54	0.64	−0.74	0.86	0.83	−0.47	0.00	0.61	0.67	0.04	0.10	−0.13	0.12	−0.81	0.68	−0.81
	(0.22)	(−0.28)	(0.25)	(−0.35)	(0.33)	(−0.53)	(0.61)	(0.61)	(−0.31)	(0.01)	(0.35)	(0.45)	(0.04)	(0.02)	(−0.09)	(0.10)	(−0.62)	(0.43)	(−0.63)
ψ^N		−0.40	0.76	—	0.57	—	0.39	—	−0.34	0.37	—	0.44	0.50	—	—	0.34	−0.40	0.34	−0.40
		(−0.05)	(0.78)	—	(0.58)	—	(0.26)	—	(−0.40)	(−0.06)	—	(0.37)	(0.39)	—	—	(0.24)	(−0.34)	(0.07)	(−0.26)
ψ^S			—	0.86	—	0.72	—	−0.34	—	−0.42	−0.58	−0.49	—	—	0.48	−0.52	0.67	−0.54	0.66
			—	(0.66)	—	0.91	—	(−0.09)	—	(−0.22)	(−0.31)	(−0.23)	—	—	(0.33)	(−0.27)	(0.34)	(−0.19)	(0.33)
$\omega^E - \omega^W$			−0.36	0.76	−0.59	0.91	−0.86	−0.66	0.33	−0.10	−0.65	−0.60	−0.17	0.11	0.43	−0.43			
			(−0.20)	(0.45)	(−0.35)	(0.62)	(−0.57)	(−0.43)	(0.14)	0.03	(−0.30)	(−0.30)	(−0.10)	(0.02)	(0.16)	(−0.21)			

and JJA. The years selected as warm or cold years are listed in Table 3. We note that some of the selected cases may not be strictly independent events because they were taken from consecutive years. The warm–cold cross sections in Fig. 8 show a beautiful symmetry with respect to the equator, with strengthened direct (i.e., energy releasing) Hadley cells [~3–4 ($\times 10^{10}$ kg s^{-1}) increase] in each hemisphere during warm ENSO conditions and weakened cells during cold conditions. On the other hand, the midlatitude Ferrel cell seems to weaken during warm ENSO conditions. We should emphasize that the anomalous Hadley circulations are superposed on the normal one-cell winter Hadley circulation in the Tropics.

3) ALTERNATIVE MEASURES OF THE HADLEY CELLS

The validity of choosing the ψ-maximum index as a measure of the strength of the Hadley cells has also been tested by comparing the above results with time series of other indexes of the Hadley cell intensity—that is, the mean upper–lower-level difference in the mean meridional velocity $[\overline{v}]_{200} - [\overline{v}]_{850}$ at 10°S and 10°N, and the 200-mb average zonal velocity $[u]_{200}$ between 15° and 25°S and 15° and 25°N. The results are presented in Table 2 for the interannual variations (see also later discussion of Figs. 9 and 10) and in appendix A (Table A2, lines 8 and 9; Table A3, lines 1 and 2) for the long-term mean conditions.

We find that the mean meridional velocity differences (from which ψ^N and ψ^S were computed) lead to similar and even slightly higher correlations than those computed based on the maximum streamfunction. As expected, if we chose the meridional velocity difference averaged only over the Pacific sector (120°E–80°W), Table 2 (columns 6 and 7) shows that the correlations tend to be higher, except for ψ^N and ψ^S. We confirm Arkin's (1982) earlier findings that during warm ENSO conditions the subtropical 200-mb jet streams u_{200} in both hemispheres tend to increase in strength and that they tend to weaken during cool anti-ENSO conditions [see also the angular momentum studies reviewed in Rosen (1993)]. The correlations are very high, with values of $r \geq 0.80$ for the smoothed time series. This suggests that the strength of the subtropical jet stream, in spite of being an indirect measure of the intensity of the maximum overturning (through the conservation of absolute angular momentum), may actually be a good indicator of the intensity of the Hadley cells. In any case, all these different measures support the validity of the results based on our streamfunction analyses.

The implications for the equatorial water and energy budgets are also presented in Table 2 (columns 10–17). The corresponding correlations show, as expected, a stronger atmospheric convergence of water vapor into the equatorial belt during ENSO conditions

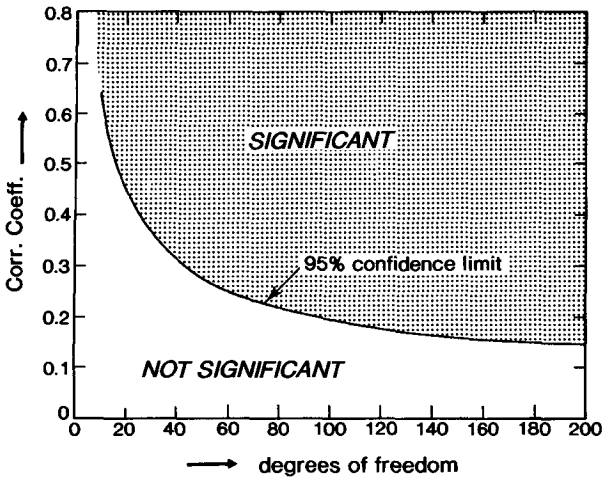

FIG. 7. A plot of the 95% confidence limit as a function of the zero-lag correlation coefficient r and the number of degrees of freedom N_{df}. All values of r above the curve are considered to be significantly different from zero at the 95% confidence limit.

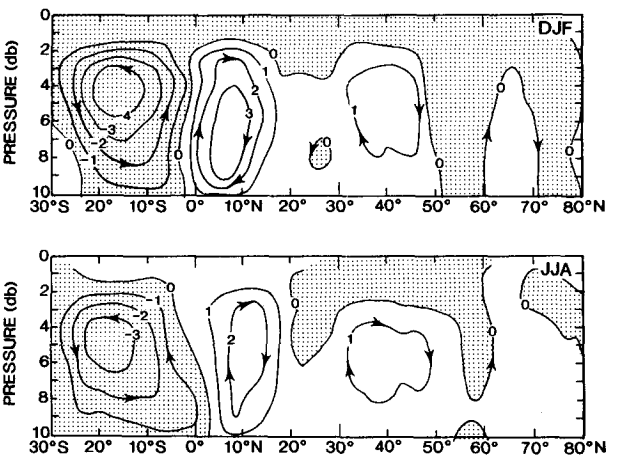

FIG. 8. Cross section of the difference in the streamfunction between the five warmest and the five coldest DJF (top) and JJA (bottom) seasons in units of 10^{10} kg s^{-1}. The difference is a measure of the range of values between El Niño and La Niña conditions. Table 3 lists the years used in these samples.

and a weaker convergence during anti-ENSO conditions. In other words, since for the 10°S–10°N belt $F_q^S - F_q^N = \int_{10S}^{10N} (P - E)dA$ (where dA is an area element), we find a clear increase of precipitation (P) over evaporation (E) during warm ENSO conditions and a decrease during cool anti-ENSO conditions, with a high value of $r = 0.67$. However, it is interesting that the corresponding correlations between ENSO and the energy divergence from the equatorial zone are insignificant.

b. *Walker–ENSO time series*

It is known from earlier research (e.g., Julian and Chervin 1978) that the rising and sinking motions associated with the west and east branches of the Walker oscillation are well correlated with the sea surface temperature anomalies in the eastern equatorial Pacific. This is confirmed in Fig. 6 (bottom diagram) in the 26-year time series of the ω_{500} difference between the eastern and western equatorial Pacific when plotted together with the sea surface temperature anomalies in the EEP region. The curves for the Walker index ($\omega_{500}^E - \omega_{500}^W$) and the SST anomalies (both smoothed) are simultaneously correlated at a highly significant value of −0.81 (see Table 2, column 20). We note that the individual time series of ω_{500}^E and ω_{500}^W are also highly correlated with the SST anomalies, as shown in Table 2 (columns 18 and 19). Clearly, a weakening of the Walker cell is accompanied by anomalous warming in the EEP region. Notice in Fig. 6 that during very strong El Niño events, particularly in 1983, the Walker index tends to change sign, indicating a reversed Walker oscillation with net rising over the eastern equatorial Pacific and sinking over the western portion. This reversal becomes obvious when we compare the 1983 value with the "normal" values of ω_{500}^E and ω_{500}^W in Table A3 (lines 11–13). The strong correlations found here (see Table 2) give a very interesting, independent measure of the ENSO phenomenon that supplements our results for the Hadley cell variations. We find in Table 2 (column 20) that the zero-lag correlations of the smoothed ψ^N and ψ^S anomalies with the Walker index are −0.40 and 0.66, respectively, indicating an out-of-phase relationship between the Hadley and Walker oscillations. The correlations at positive and negative lag (not presented) are smaller and fairly symmetrical, indicating an almost simultaneous occurrence of these two aspects of the ENSO phenomenon.

To show better the three-dimensional structure of the ENSO phenomenon as it appears in our data, we have prepared in Figs. 9 and 10 some horizontal difference maps between warm (ENSO) and cold (anti-ENSO) conditions, similar to those shown in

TABLE 3. Selected five warmest and five coldest DJF and JJA seasons used in computing Figs. 8–10. The selection of warm and cold seasons is based on the time series of the sea surface temperature in the eastern equatorial Pacific.

Warm DJF	Cold DJF	Warm JJA	Cold JJA
1968–69	1964–65	1965	1964
1972–73	1970–71	1972	1971
1982–83	1973–74	1982	1973
1986–87	1974–75	1983	1975
1987–88	1975–76	1987	1988

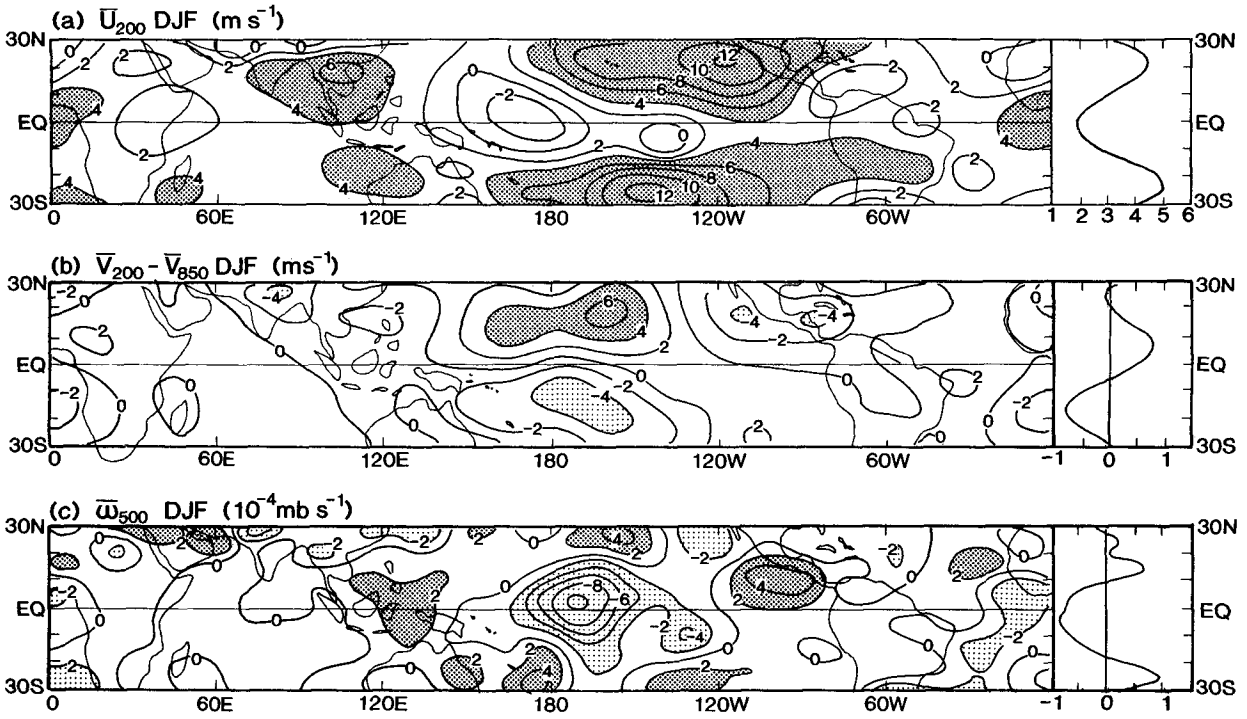

FIG. 9. Horizontal distributions of the warm–cold differences in the tropical belt between 30°N and 30°S during DJF for the quantities (a) $\bar{u}_{200}$ in units of m s^{-1}, (b) $\bar{v}_{200} - \bar{v}_{850}$ in units of m s^{-1}, and (c) $\bar{\omega}_{500}$ in units of 10^{-4} mb s^{-1}.

Fig. 8 for the streamfunction. In Figs. 9a and 10a the $\bar{u}_{200}$ differences are presented for DJF and JJA conditions, respectively. They show the strengthening of the subtropical jet streams and the occurrence of anomalous easterly winds ($\bar{u}_{200} < 0$) over the western equatorial Pacific Ocean, representing the upper branch of the reversed Walker oscillation. However, it should be noted that part of the $\bar{u}_{200}$ and $\bar{v}_{200}$ anomalies are connected with the rotational component of the flow around the (also ENSO connected) upper-level anticyclones straddling the equator (see, e.g., Arkin 1982) and are, therefore, not connected directly with the divergent component of the response or with the anomalies in the $\bar{\omega}$ field. In Figs. 9b and 10b the local contributions to the Hadley cells are shown in terms of $\bar{v}_{200} - \bar{v}_{850}$. The main strengthening (weakening) of the Hadley cells during ENSO (anti-ENSO) conditions is apparently due to the increases (decreases) over the western and central Pacific, in good agreement with earlier research. Finally, in Figs. 9c and 10c, the $\bar{\omega}_{500}$ differences show anomalous rising ($\omega_{500} < 0$) over the central and eastern equatorial Pacific (especially strong during the northern winter) and sinking ($\omega_{500} > 0$) over the Indonesian Archipelago, again indicating a reversal of the normal Walker oscillation. In addition, zonal-mean profiles are shown on the right-hand side of each figure. These ENSO-related effects are about a factor 5 to 10 smaller than the corresponding climatological values given in Tables A2 and A3.

5. Summary

Some of the main results of our analyses based on a 26-yr sample of consistently analyzed monthly mean analyses of the zonal and meridional wind components are the following.

- The normal seasonal cycle in the tropical Hadley cells determined here is very similar to that found in earlier studies which shows the robustness of our results.
- The seasonal extreme values in ψ are found in winter at about 8° latitude, with maximum values of 22 $\times 10^{10}$ kg s^{-1} near the 450-mb level in the NH, and 18 $\times 10^{10}$ kg s^{-1} near the 600-mb level in the SH. The summer maxima in ψ are quite weak (less than 5 $\times 10^{10}$ kg s^{-1}), occur near 25° latitude, and are not well defined.
- Superposed on the normal one-cell tropical winter Hadley circulation, we find two strengthened direct Hadley cells during warm ENSO conditions and weakened cells during cold anti-ENSO conditions. The warm–cold strengthening of the Hadley cells is ~3–4 ($\times 10^{10}$ kg s^{-1}), whereas the midlat-

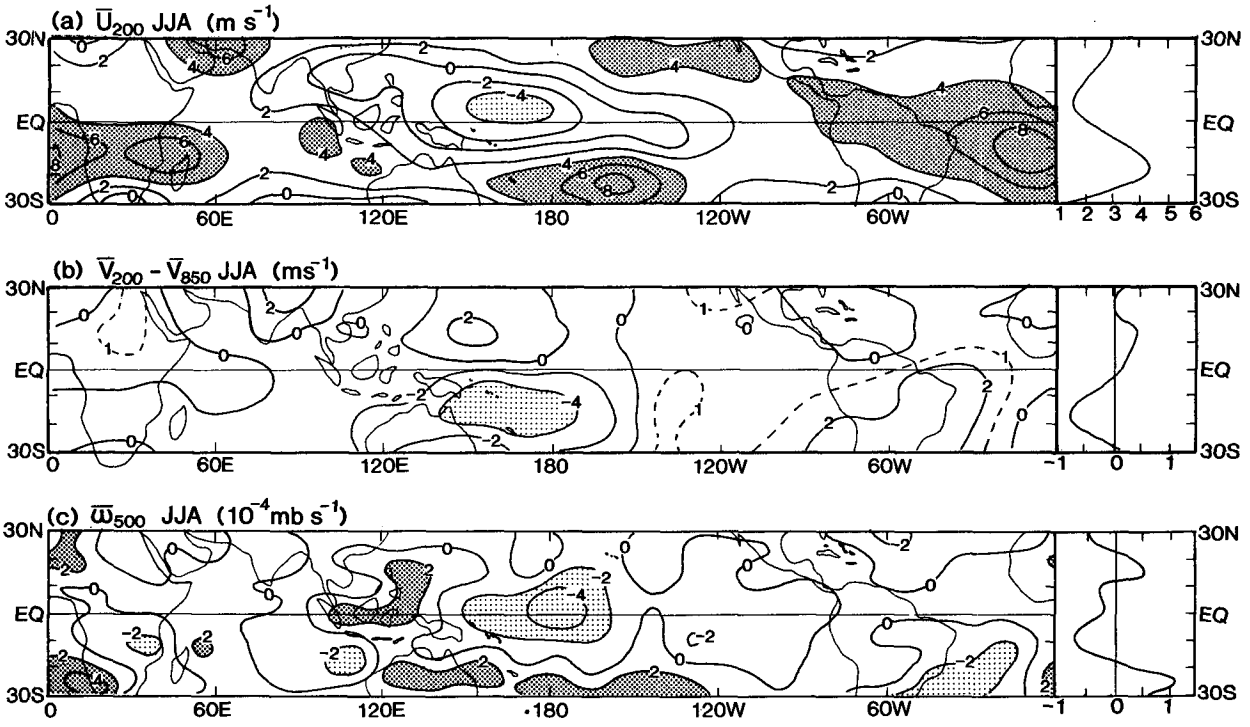

FIG. 10. The same as in Fig. 9 but for JJA.

itude Ferrel cell tends to weaken by about 1×10^{10} kg s^{-1}.

• Consistent results are found when some other quantities are considered, such as the $\bar{v}_{200} - \bar{v}_{850}$ difference, the water vapor flux, and the $\bar{u}_{200}$ fields. For example, the inferred equatorial $P-E$ values increase (decrease) during warm (cold) conditions ($r \approx 0.7$), consistent with the strengthening (weakening) of the Hadley cells. Also, the u_{200} correlations show a strengthening (weakening) of the subtropical jets during warm (cold) conditions, with $r \approx 0.8$.

• The Walker oscillation weakens during ENSO when the anomalous Hadley cells are stronger and strengthens during anti-ENSO conditions when they are weaker. The correlations with T_S^{EEP} are very high ($r \approx -0.8$). The inverse relationship between the Hadley and Walker oscillations on the ENSO timescale is clearly evident.

Acknowledgments. We are grateful to Isaac Held, Gabriel Lau, Richard Rosen, and the official reviewers for their comments improving the manuscript; to Yoshi Hayashi for drawing our attention to Mitchell's method for estimating the number of degrees of freedom; to Andrzej Klonecki, John Lanzante, and De-Zheng Sun for various useful suggestions; to Cathy Raphael and Jeff Varanyak for drafting the figures; and to Wendy Marshall for typing the manuscript.

APPENDIX A

Supplementary Tables

This appendix contains tables that give additional information for a proper perspective of the results shown in sections 3 and 4. The information should also prove useful for comparisons with simple models, as well as general circulation models, trying to simulate the annual cycle of the tropical Hadley cells.

First, Table A1 lists and defines the symbols and notations used in the main text for the various measures of the ENSO signal, the tropical Hadley cells, and the Walker oscillation.

Then Tables A2 and A3 give the long-term mean values and the interannual standard deviations (in parentheses) of the various quantities defined in Table A1. The values are presented both for the 12 calendar months and the annual mean.

Various types of "mean" values are shown in Table A2 for the quantities associated with the maximum streamfunctions ψ^{N} and ψ^{S}. Specifically, we should note in Table A2 that there are 3 lines of estimates for characteristics of the maximum in the streamfunction (quantities 2–7). The first line shows the mean of the 26 yearly values, the second line its interannual standard deviation (in parentheses), and the third line the value for the 26-yr mean streamfunction (in italics). The numbers in the third line correspond to the estimates one would infer by looking at Figs. 2 and 3.

TABLE A1. List of symbols and their meaning as used in the paper.

Measure of strength of ENSO signal:

$T_S \equiv \int_{-20°}^{20°} \int_{-180°}^{-80°} T_S R^2 \cos\phi d\lambda d\phi / \int_{-20°}^{20°} \int_{-180°}^{-80°} R^2 \cos\phi d\lambda d\phi$ = mean sea surface temperature in eastern equatorial Pacific, where R is the mean radius of the earth, λ is longitude, and ϕ is latitude

Measures of strength of NH Hadley cell:

$\psi^N \equiv$ maximum value of streamfunction in 0°–30°N region

$\Delta v^N \equiv [\bar{v}_{200}] - [\bar{v}_{850}]$ at 10°N

$\Delta v^N_{PAC} \equiv \bar{v}_{200} - \bar{v}_{850}$ averaged over Pacific longitude sector 120°E–80°W along 10°N

$u^N_{200} \equiv \int_{15°N}^{25°N} [\bar{u}_{200}] \cos\phi d\phi / \int_{15°N}^{25°N} \cos\phi d\phi$ = strength of subtropical jet

$F^N_q \equiv 2\pi R \cos\phi \int_0^{p_0} [\bar{v}][\bar{q}] dp/g$ at 10°N = northward flux of water vapor across 10°N associated with NH Hadley cell

$F^N_E \equiv 2\pi R \cos\phi \int_0^{p_0} [\bar{v}][\bar{E}] dp/g$ at 10°N = northward flux of total energy across 10°N associated with NH Hadley cell, where $E = c_p T + gz + Lq + \frac{1}{2}(u^2 + v^2)$

Measures of strength of SH Hadley cell:

$\psi^S \equiv$ maximum value of streamfunction in 30°S–0° region

$\Delta v^S \equiv [\bar{v}_{200}] - [\bar{v}_{850}]$ at 10°S

$\Delta v^S_{PAC} \equiv \bar{v}_{200} - \bar{v}_{850}$ averaged over Pacific longitude sector 120°E–80°W along 10°S

$u^S_{200} \equiv \int_{-25°}^{-15°} [\bar{u}_{200}] \cos\phi d\phi / \int_{-25°}^{-15°} \cos\phi d\phi$ = strength of subtropical jet

$F^S_q \equiv 2\pi R \cos\phi \int_0^{p_0} [\bar{v}][\bar{q}] dp/g$ at 10°S = northward flux of water vapor across 10°S associated with SH Hadley cell

$F^S_E \equiv 2\pi R \cos\phi \int_0^{p_0} [\bar{v}][\bar{E}] dp/g$ at 10°S = northward flux of total energy across 10°S associated with NH Hadley cell where $E = c_p T + gz + Lq + \frac{1}{2}(u^2 + v^2)$

Measures of strength of Walker Oscillation:

$\omega^E_{500} \equiv \int_{-10°}^{10°} \int_{-180°}^{-100°} \bar{v}_{500} \cos\phi d\lambda d\phi / \int_{-10°}^{10°} \int_{-180°}^{-100°} \cos\phi d\lambda d\phi$ = mean sinking motion at 500 mb over eastern equatorial Pacific

$\omega^W_{500} \equiv \int_{-10°}^{10°} \int_{100°}^{150°} \bar{\omega}_{500} \cos\phi d\lambda d\phi / \int_{-10°}^{10°} \int_{100°}^{150°} \cos\phi d\lambda d\phi$ = mean sinking motion at 500 mb over Indian Ocean and western equatorial Pacific

Measure of combined strength of NH and SH Hadley cells:

$P - E \equiv (F^S_q - F^N_q) / \int_{-10°}^{10°} 2\pi R^2 \cos\phi d\phi$ = mean precipitation minus evaporation rate over equatorial zone

$\mathrm{div}\vec{F}_E \equiv (F^N_E - F^S_E) / \int_{-10°}^{10°} 2\pi R^2 \cos\phi d\phi$ = mean divergence of total energy over equatorial zone

Comparing lines 1 and 3, we find, as expected (see discussion below), that the values for ψ^N and ψ^S are slightly smaller when the 26-yr mean picture (line 3) is considered, especially for the annual mean. We also note that the pressure estimates for the 26-year mean are truncated to multiples of 50 mb because of the use of 50-mb intervals in our analyses.

To explain the importance of differentiating between the various means, let us consider ψ^N for the column labeled *mean*. The first entry 11.6 represents the mean of the 312 values for the individual months, whereas the third entry 9.1 in the column labeled *annual* indicates the maximum ψ for the 0°–30°N zone in the 26-yr annual-mean cross section. Because we always select the maximum streamfunction irrespective of latitude and pressure within the 0°–30°N sector, the one long-term average cross section of ψ must yield a lower maximum value than the mean for the 312 individual cross sections. In other words, the mean of the maxima in the 312 streamfunctions must be larger than the maximum in the 26-yr mean streamfunction.

Similarly, we note that the streamfunction maxima for the *mean* are located farther removed from the equator (at 12°N and −10°S). This is due to the fact that the strongest ψ^N and ψ^S always occur in winter at low latitudes, whereas the weakest ψ^N and ψ^S occur in summer far away from the equator.

The information in Tables A2 and A3 gives a comprehensive picture of the observed annual cycle of the Hadley and Walker circulations. Table A2 clearly shows the seasonal waning and waxing of the tropical cells (lines 2, 3, 8, and 9), their latitudinal migration (lines 4 and 5), and their growth and collapse in the vertical (lines 6 and 7).

Table A3 gives the implied response of the Hadley cells in terms of the strength of the tropical jet stream (lines 1 and 2), the northward flux of water vapor (lines 3–5), the excess of precipitation over evapo-

TABLE A2. Estimates of the 26-yr mean (1964–89) and interannual standard deviation (in parentheses) values for various quantities related to the ENSO cycle (No. 1), and the Hadley circulation (No. 2–9). In the case of the Hadley circulation, quantities 2–9 relate to the maximum strength of the mass overturning and the latitude and pressure level where the maximum occurs. Shown are the values for the 12 individual calendar months, the annual case (column labeled *annual*), and the 12-month average (column labeled *mean*). Each mean and standard deviation estimate is based on 26 values in the case of the calendar months and the annual, but on 312 monthly values in the case of the values in the column labeled *mean*. For quantities 2–7, the third row of numbers (in italics) indicates the characteristics of the maximum in the 26-yr mean streamfunction, which is generally different from the corresponding mean of the 26 individual values (see text).

	January	February	March	April	May	June	July	August	September	October	November	December	Annual	Mean[a]	Units
1. T_S^{EEP}	26.3	26.6	26.9	27.0	27.0	26.7	26.3	26.1	26.1	26.1	26.1	26.1	26.4	26.4	°C
	(0.6)	(0.4)	(0.4)	(0.3)	(0.4)	(0.4)	(0.4)	(0.4)	(0.5)	(0.5)	(0.5)	(0.6)		(0.4)	
2. ψ^N	22.9	22.9	19.4	15.4	5.5	2.0	1.4	2.1	4.7	8.2	13.8	20.8	9.2	11.6	10^{10} kg s^{-1}
	(2.7)	(3.1)	(2.1)	(2.4)	(2.1)	(1.3)	(0.7)	(1.1)	(1.2)	(1.6)	(2.2)	(2.7)		(2.1)	
	21.9	*22.1*	*18.8*	*15.2*	*4.9*	*0.8*	*0.9*	*1.2*	*4.0*	*8.0*	*13.5*	*20.2*	*9.1*	*10.9*	
3. ψ^S	−3.1	−3.3	−4.2	−7.3	−14.2	−17.4	−19.3	−18.4	−16.1	−10.0	−5.3	−3.2	−7.4	−10.2	10^{10} kg s^{-1}
	(1.2)	(1.0)	(1.4)	(1.7)	(1.9)	(2.6)	(2.4)	(2.1)	(2.4)	(2.7)	(2.0)	(1.2)		(2.0)	
	−2.2	*−2.6*	*−3.5*	*−6.8*	*−13.8*	*−17.0*	*−18.7*	*−18.1*	*−15.8*	*−9.5*	*−4.6*	*−2.7*	*−7.3*	*−9.6*	
4. $\phi(\psi^N)$	8	7	9	10	12	25	26	26	29	16	12	10	12	16	°lat
	(3)	(2)	(1)	(1)	(3)	(8)	(6)	(9)	(5)	(2)	(1)	(2)		(4)	
	8	*8*	*8*	*10*	*12*	*30*	*26*	*32*	*32*	*16*	*12*	*10*	*12*	*(17)*	
5. $\phi(\psi^S)$	−27	−27	−22	−13	−8	−8	−7	−7	−6	−7	−13	−19	−9	−13	°lat
	(6)	(5)	(7)	(3)	(1)	(2)	(2)	(2)	(2)	(1)	(5)	(6)		(4)	
	−26	*−26*	*−20*	*−12*	*−8*	*−8*	*−6*	*−6*	*−6*	*−6*	*−12*	*−16*	*−10*	*−13*	
6. $p(\psi^N)$	462	446	475	477	533	585	698	617	623	596	602	494	552	551	mb
	(105)	(106)	(99)	(64)	(127)	(268)	(259)	(218)	(109)	(85)	(80)	(105)		(152)	
	400	*400*	*400*	*500*	*550*	*700*	*900*	*800*	*650*	*600*	*600*	*550*	*550*	*588*	
7. $p(\psi^S)$	731	877	827	777	648	612	594	617	585	613	790	877	742	712	mb
	(283)	(25)	(118)	(42)	(71)	(100)	(94)	(62)	(68)	(109)	(143)	(98)		(119)	
	900	*900*	*900*	*750*	*650*	*650*	*600*	*600*	*600*	*650*	*850*	*900*	*750*	*746*	
8. Δv^N	5.2	5.4	4.4	3.2	0.3	−1.0	−1.5	−1.7	−0.7	0.8	2.9	4.7	1.8		m s^{-1}
	(0.7)	(0.8)	(0.4)	(0.5)	(0.5)	(0.5)	(0.4)	(0.5)	(0.5)	(0.4)	(0.5)	(0.6)	(0.6)		
9. Δv^S	2.1	1.9	0.7	−1.0	−2.8	−3.8	−4.0	−3.8	−3.0	−1.8	−0.3	1.2	−1.2		m s^{-1}
	(0.9)	(0.5)	(0.6)	(0.5)	(0.5)	(0.7)	(0.6)	(0.6)	(0.7)	(0.6)	(0.7)	(0.8)	(0.6)		

[a] The mean and standard deviation values in this column are computed from the full sample of 26 × 12 = 312 months. The normal annual cycle was removed before the standard deviation values were computed.

TABLE A3. Estimates of the 26-yr mean (1964–89) and interannual standard deviation values (in parentheses) for various quantities related (indirectly) to the Hadley circulation (lines 1–10) and to the Walker Oscillation (lines 11–13). Also see Table A2 caption.

	January	February	March	April	May	June	July	August	September	October	November	December	Annual	Units
1. u^{N}_{200}	25.7	26.9	26.1	23.2	14.8	2.2	−4.2	−3.8	0.1	8.3	15.9	21.8	13.1	m s^{-1}
	(2.6)	(2.9)	(2.4)	(1.5)	(1.7)	(1.5)	(1.3)	(1.2)	(1.5)	(1.7)	(1.8)	(1.7)	(1.9)	
2. u^{S}_{200}	6.7	5.2	8.2	16.7	23.3	24.2	23.3	22.5	22.2	21.6	18.7	12.7	17.1	m s^{-1}
	(2.9)	(2.4)	(2.2)	(2.3)	(1.8)	(2.4)	(2.4)	(2.6)	(2.5)	(2.1)	(2.1)	(2.8)	(2.4)	
3. F^{N}_{q}	−23.6	−22.7	−20.0	−16.3	−6.8	2.2	6.9	9.4	6.2	−5.0	−16.2	−21.9	−9.0	10^{8} kg s^{-1}
	(2.8)	(2.2)	(2.3)	(1.7)	(2.3)	(2.1)	(2.4)	(3.1)	(3.0)	(2.1)	(2.2)	(2.7)	(2.4)	
4. F^{eq}_{q}	−11.4	−14.0	−8.7	0.8	15.3	20.3	22.4	21.4	19.2	13.2	4.6	−4.9	6.5	10^{8} kg s^{-1}
	(3.1)	(2.9)	(3.4)	(3.1)	(2.6)	(2.6)	(2.6)	(1.7)	(2.4)	(1.6)	(2.2)	(2.1)	(2.6)	
5. F^{S}_{q}	−3.1	−3.9	3.2	11.5	17.3	18.6	20.1	18.6	16.7	11.6	7.2	0.5	9.9	10^{8} kg s^{-1}
	(3.1)	(2.4)	(2.1)	(2.2)	(2.1)	(2.2)	(2.3)	(2.2)	(1.9)	(2.0)	(2.1)	(2.6)	(2.3)	
6. $P - E$	0.73	0.67	0.83	0.99	0.86	0.58	0.47	0.33	0.37	0.59	0.83	0.79	0.67	m yr^{-1}
	(0.17)	(0.11)	(0.10)	(0.08)	(0.12)	(0.11)	(0.11)	(0.14)	(0.12)	(0.11)	(0.12)	(0.16)	(0.12)	
7. F^{N}_{E}	2.9	2.4	1.9	1.0	0.2	−0.2	−0.5	−0.7	−0.4	0.4	1.1	2.2	0.9	10^{15} W
	(0.6)	(0.5)	(0.6)	(0.4)	(0.4)	(0.4)	(0.5)	(0.5)	(0.4)	(0.4)	(0.5)	(0.7)	(0.5)	
8. F^{eq}_{E}	2.3	2.1	0.9	0.4	−0.8	−1.2	−1.6	−1.7	−1.6	−0.5	0.4	1.6	0.0	10^{15} W
	(0.6)	(0.6)	(0.5)	(0.4)	(0.5)	(0.6)	(0.6)	(0.6)	(0.5)	(0.6)	(0.5)	(0.6)	(0.5)	
9. F^{S}_{E}	0.5	1.6	0.6	0.2	−1.3	−1.6	−2.4	−2.1	−1.8	−0.8	−0.2	0.5	−0.6	10^{15} W
	(0.5)	(0.5)	(0.5)	(0.4)	(0.6)	(0.6)	(0.5)	(0.6)	(0.7)	(0.6)	(0.5)	(0.6)	(0.6)	
10. divF_{E}	26	9	15	9	17	16	22	16	16	13	15	19	16	W m^{-2}
	(10)	(8)	(8)	(6)	(9)	(8)	(8)	(9)	(7)	(8)	(7)	(7)	(8)	
11. ω^{E}_{500}	1.9	1.3	1.4	0.3	0.5	0.5	0.0	0.1	0.2	0.6	0.9	1.0	0.7	10^{-4} mb s^{-1}
	(1.9)	(1.6)	(1.4)	(1.0)	(0.7)	(0.8)	(0.8)	(1.0)	(1.0)	(1.1)	(1.3)	(1.8)	(1.3)	
12. ω^{W}_{500}	−3.0	−2.6	−3.2	−2.5	−2.5	−3.1	−2.3	−2.0	−1.8	−2.5	−3.5	−3.4	−2.7	10^{-4} mb s^{-1}
	(0.9)	(1.0)	(1.1)	(0.8)	(0.7)	(0.9)	(1.0)	(1.1)	(1.2)	(1.4)	(1.3)	(1.1)	(1.1)	
13. $\omega^{E}_{500} - \omega^{W}_{500}$	4.9	3.9	4.5	2.8	3.0	3.6	2.3	2.1	2.0	3.1	4.4	4.4	3.4	10^{-4} mb s^{-1}
	(2.5)	(2.4)	(2.0)	(1.4)	(1.2)	(1.4)	(1.5)	(1.5)	(1.9)	(2.2)	(2.3)	(2.5)	(1.9)	

ration in the equatorial zone (line 6), the northward flux of total energy (geopotential energy + sensible heat + latent heat + kinetic energy) (lines 7–9), and the atmospheric divergence of total energy from the equatorial zone (line 10). Finally, Table A3 supplies information on the seasonal variability in the east and west branches of the Walker oscillation (lines 11–13).

APPENDIX B

Mitchell's Method for Estimating the Number of Degrees of Freedom

Since the method used in this paper to estimate the number of degrees of freedom does not seem to be known in the meteorological literature, we repeat here the derivation by the late J. Murray Mitchell Jr. (1963, unpublished manuscript). We may note that, as far as we know, only in the case of the *autocorrelation* of a time series have similar derivations for the number of degrees of freedom been presented (see, e.g., Jones 1975). Mitchell presented this material at the 44th Annual Meeting of the American Geophysical Union in Washington, D.C., 17–20 April 1963 in a talk entitled "Some Practical Considerations in the Analysis of Geophysical Time Series." It is an extension of the work on standard tests of significance by a World Meteorological Organization Working Group under his chairmanship [WMO (1966), see especially Eq. (18) and related discussion].

Sampling error of the correlation coefficient

When two time series ($x_1, x_2, \ldots, x_N$ and $y_1, y_2, \ldots, y_N$) are *cross*-correlated and both series are *autocorrelated,* the sampling distribution of the cross-correlation coefficient $r(x, y)$ around its population value $\rho(x, y)$ is generally influenced by the autocorrelations [$\rho_\tau(x)$ and $\rho_\tau(y)$].

Since the autocorrelation ρ_τ for an arbitrary lag τ in the population is not known, it can be estimated directly from the sample series by the expression

$$r_\tau = \sum_{i=1}^{N-\tau} \frac{(x_i - \bar{x})(x_{i+\tau} - \bar{x})}{(N-\tau)s_1^2(x)}, \tag{B1}$$

where $s_1^2(x) \equiv (N-1)s^2(x)/N$, and $s(x)$ is the estimated standard deviation

$$s(x) = \left(\frac{1}{N-1}\sum_{i=1}^{N}(x_i - \bar{x})^2\right)^{1/2}. \tag{B2}$$

For convenience, let the population means of the two (stationary) variates x and y each be zero. Then, for our samples ($x_1, x_2, \ldots, x_N$ and $y_1, y_2, \ldots, y_N$) the expected values $E\{x_i\} = E\{y_i\} = 0$ for all $i = 1, 2, \cdots, N$. The population cross-correlation coefficient $\rho(x, y)$ is given by the expected value of the sample coefficient $r(x, y)$:

$$\rho(x, y) = E\{r(x, y)\} = E\left\{\frac{c(x, y)}{s_1(x)s_1(y)}\right\}, \tag{B3}$$

where

$$c(x, y) = \frac{1}{N}\sum_{i=1}^{N} x_i y_i \tag{B4}$$

is the sample covariance.

If we stipulate (for the population) that $\rho(x_i, y_i) = 0$ ($i = j$ and $i \neq j$), a measure of the sampling distribution of $r(x, y)$ around its expected value (zero) is given by

$$E\{r^2(x, y)\} = E\left\{\frac{c^2(x, y)}{s_1^2(x)s_1^2(y)}\right\} \approx \frac{E\{c^2(x, y)\}}{\sigma^2(x)\sigma^2(y)}. \tag{B5}$$

In general,

$$c^2(x, y) = \left[\frac{1}{N}\sum_{i=1}^{N} x_i y_i\right]^2 = \frac{1}{N^2}\left[\sum_{i=1}^{N} x_i^2 y_i^2 + 2\sum_{\substack{i,j=1 \\ j>i}}^{N} x_i y_i x_j y_j\right], \tag{B6}$$

since $\rho(x_i, y_i) = 0$, $E\{x_i y_i\} = 0$ for all i and j, and the expected value of (B6) becomes

$$E\{c^2(x, y)\} = \frac{\sigma^2(x)\sigma^2(y)}{N} + \frac{2}{N^2}E\left\{\sum_{\substack{i,j=1 \\ j>i}}^{N} x_i x_j y_i y_j\right\}. \tag{B7}$$

Applying (B1) separately to x and y, allowing $\bar{x}$ and $\bar{y}$ to assume their expected values of zero, and defining $j - i = \tau$, we may write (B7) as

$$E\{c^2(x, y)\} = \frac{\sigma^2(x)\sigma^2(y)}{N}\times\left[1 + \frac{2}{N}\sum_{\tau=1}^{N-1}(N-\tau)\rho_\tau(x)\rho_\tau(y)\right], \tag{B8}$$

in which $\rho_\tau(x)$ and $\rho_\tau(y)$ are the population autocorrelation values of x and y, respectively, for lag τ.

With (B8), (B5) becomes

$$E\{r^2(x, y)\} \approx \frac{1}{N}\left[1 + \frac{2}{N}\sum_{\tau=1}^{N-1}(N-\tau)\rho_\tau(x)\rho_\tau(y)\right]. \tag{B9}$$

To clarify the significance of this result, we can set $\rho_\tau(x) = 0$ and/or $\rho_\tau(y) = 0$, by which we stipulate that the x_i and/or y_i series are random. In this event, (B9) reduces to

$$E\{r^2(x, y)\}_R \approx 1/N, \tag{B10}$$

where the subscript R identifies the assumption of randomness. At this stage we may introduce the concept of effective sample size. We ask, what value of N in (B10)—call this the number of degrees of freedom N_{df}—will yield the same value of $E\{r^2(x, y)\}$ as (B9) yields and is appropriate to the case of autocorrelation in the two series being cross correlated?

It follows that, to a good approximation, N_{df} can be estimated as

$$N_{df} = N\left[1 + \frac{2}{N}\sum_{\tau=1}^{N-1}(N-\tau)\rho_\tau(x)\rho_\tau(y)\right]^{-1}. \quad \text{(B11)}$$

In (B11) the population autocorrelation coefficients can be replaced with acceptable accuracy by the sample coefficients $r_\tau(x)$ and $r_\tau(y)$ calculated from the series at hand, so that

$$N_{df} = N\left[1 + \frac{2}{N}\sum_{\tau=1}^{N-1}(N-\tau)r_\tau(x)r_\tau(y)\right]^{-1}. \quad \text{(B12)}$$

It should be noted from (B9) that in order for the autocorrelation to influence the error of estimate of the cross correlation between two series, *both* series must be autocorrelated (i.e., both series must be nonrandom).

The value of N_{df} given by (B11) is to be regarded as the appropriate number of pairs of observations for use in our tests of significance of the correlation coefficients.

REFERENCES

Arkin, P. A., 1982: The relationship between interannual variability in the 200-mb tropical wind field and the Southern Oscillation. *Mon. Wea. Rev.*, **110,** 1393–1404.

Bjerknes, J., 1969: Atmospheric teleconnections from the equatorial Pacific. *Mon. Wea. Rev.*, **97,** 163–172.

Jones, R. H., 1975: Estimating the variance of time averages. *J. Appl. Meteor.*, **14,** 159–163.

Julian, P. R., and R. M. Chervin, 1978: A study of the Southern Oscillation and Walker circulation phenomena. *Mon. Wea. Rev.*, **106,** 1433–1451.

Newell, R. E., J. W. Kidson, D. G. Vincent, and G. J. Boer, 1972: *The General Circulation of the Tropical Atmosphere.* Vol. 1. The MIT Press, 258 pp.

Oort, A. H., 1983: Global atmospheric circulation statistics, 1958–1973. NOAA Prof. Paper 14, 180 pp. and 47 microfiche. [Available from author at GFDL/NOAA, P.O. Box 308, Princeton, NJ 08542.]

——, and E. M. Rasmusson, 1970: On the annual variation of the monthly mean meridional circulation. *Mon. Wea. Rev.*, **98,** 423–442.

Pan, Y. H., and A. H. Oort, 1983: Global climate variations connected with sea surface temperature anomalies in the eastern equatorial Pacific Ocean for the 1958–73 period. *Mon. Wea. Rev.*, **111,** 1244–1258.

Peixoto, J. P., and A. H. Oort, 1992: *Physics of Climate.* American Institute of Physics, 520 pp.

Rasmusson, E. M., and T. H. Carpenter, 1982: Variations in tropical sea surface temperature and surface wind fields associated with the Southern Oscillation/El Niño. *Mon. Wea. Rev.*, **110,** 354–384.

Raval, A., A. H. Oort, and V. Ramaswamy, 1994: Observed dependence of outgoing longwave radiation on sea surface temperature and moisture. *J. Climate,* **7,** 807–821.

——, ——, and J. R. Lanzante, cited 1996: A new interpolation routine ("ANAL95") for obtaining global fields from irregularly spaced meteorological data. [Available on-line from http://www.gfdl.gov/.]

Rosen, R. D., 1976: The flux of mass across latitude walls in the atmosphere. *J. Geophys. Res.*, **81,** 2001–2002.

——, 1993: The axial momentum balance of earth and its fluid envelope. *Surv. Geophys.*, **14,** 1–29.

——, M.-F. Wu, and J. P. Peixoto, 1976: Observational study of the interannual variability in certain features of the general circulation. *J. Geophys. Res.*, **81,** 6383–6389.

——, D. A. Salstein, and J. P. Peixoto, 1979: Variability in the annual fields of large-scale atmospheric water vapor transport. *Mon. Wea. Rev.*, **107,** 26–37.

Spiegel, M. R., 1961: *Statistics.* Schaum's Outline Series in Mathematics, McGraw Hill, 359 pp.

Starr, V. P., J. P. Peixoto, and N. E. Gaut, 1970: Momentum and zonal kinetic energy balance of the atmosphere from five years of hemispheric data. *Tellus,* **22,** 251–274.

WMO, 1966: Climatic change. World Meteorological Organization Tech. Note No. 79, 79 pp. [Available from WMO Secretariat, Case Postale No. 2300, 1211 Geneva, Switzerland.]

Woodruff, S. D., R. J. Slutz, R. L. Jenne, and P. M. Steurer, 1987: A Comprehensive Ocean–Atmosphere Data Set. *Bull. Amer. Meteor. Soc.*, **68,** 1239–1250.